

Excitation of Biomolecules with Incoherent Light: Quantum yield for the photoisomerization of model retinal

T. V. Tscherbul and P. Brumer

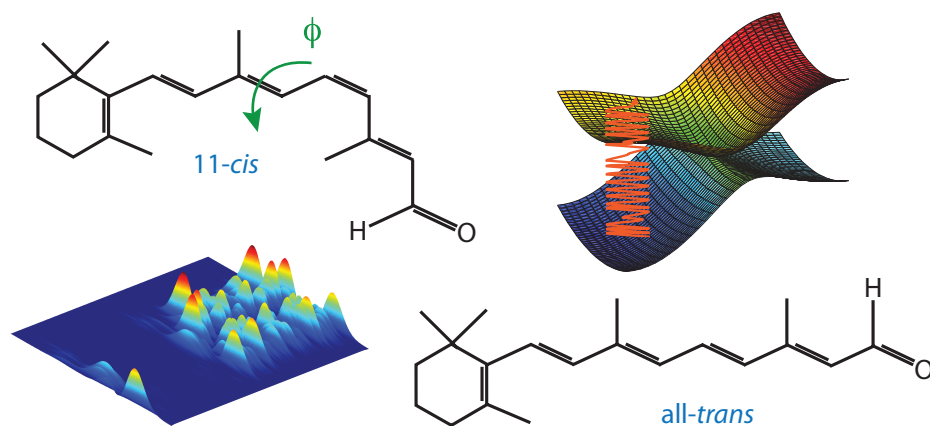
*Chemical Physics Theory Group, Department of Chemistry,
and Center for Quantum Information and Quantum Control,
University of Toronto, Toronto, Ontario, M5S 3H6, Canada**

(Dated: November 25, 2021)

Abstract

Cis-trans isomerization in retinal, the first step in vision, is often computationally studied from a time dependent viewpoint. Motivation for such studies lies in coherent pulsed laser experiments that explore the isomerization dynamics. However, such biological processes take place naturally in the presence of incoherent light, which excites a non-evolving mixture of stationary states. Here the isomerization problem is considered from the latter viewpoint and applied to a standard two-state, two-mode linear vibronic coupling model of retinal that explicitly includes a conical intersection between the ground and first excited electronic states. The calculated quantum yield at 500 nm agrees well with both the previous time-dependent calculations of Hahn and Stock (0.63) and with experiment (0.65 ± 0.01), as does its wavelength dependence. Significantly, the effects of environmental relaxation on the quantum yield in this well-established model are found to be negligible. The results make clear the connection of the photoisomerization quantum yield to properties of stationary eigenstates, providing alternate insights into conditions for yield optimization.

TOC graphic



I. INTRODUCTION

Light-induced 11-*cis* \rightarrow all-*trans* isomerization in retinal is a paradigmatic example of an important ultrafast photochemical reaction in biology¹⁻⁸. The photoreaction is the first step in dim-light vision, and its high quantum yield, and formation of all-*trans* product within 200 fs, contribute to the high efficiency of the phototransduction cascade^{1-4,6,8}. The importance of retinal photoisomerization has made its mechanism the subject of numerous experimental and computational studies. A related biological process, *cis-trans* isomerization in Retinoic Acid, has become of increasing interest in its role in zebrafish hindbrain development⁹.

To study retinal dynamics, current pump-probe experiments use ultrashort femtosecond laser pulses to excite the retinal from the ground (S_0) to the first excited (S_1) electronic state. The subsequent isomerization dynamics is then followed using a series of probe pulses, providing important insights into the sub-200 fs timescale of photoproduct formation^{2,3}, the coherent dynamics of all-*trans* photoproduct², and most recently, the role of conical intersections in determining the reaction rate³. Significantly, retinal photoisomerization occurs with high quantum yield ($Y = 0.65 \pm 0.01$), making the first step in visual phototransduction highly efficient¹⁰. Measurements of the quantum yield $Y(\lambda)$ as a function of excitation wavelength λ show a maximum at 500 nm and a small decline of $\sim 5\%$ as the laser wavelength increases from 500 nm to 570 nm^{11,12}.

A detailed time-dependent computational study of retinal photoisomerization using a multilevel Redfield theory^{4,6,8} based on a minimal two-state, two-mode (2D) model of retinal chromophore⁴ provided insights into the role of avoided crossings, conical intersections, and dissipative dynamics in ultrafast energy conversion in biomolecules⁶. In addition, they qualitatively reproduce many salient features of isomerization dynamics of retinal in rhodopsin, including the high quantum yield. There and elsewhere the quantum yield is defined dynamically, as the probability of forming the all-*trans* product starting from the initial *cis* wavepacket created by an ultrafast Franck-Condon excitation from the ground *cis* state.

This time-dependent wavepacket view^{1,11,12} is well-suited to describe time-domain experiments on rhodopsin, in which ultrafast $S_0 \rightarrow S_1$ excitation creates a wavepacket on a highly excited state. However, in nature, the excitation involves natural light. Such light has a very short coherence time (1.32 fs for sunlight) compared to the fs laser pulses used experimentally^{2,3}, and is incident on the molecule for a far longer time. As a result, after some time, which is dependent on a number of conditions¹³⁻¹⁵, the molecule is prepared in a mixture of stationary states that exhibits no coherent

time evolution^{16,17}. Furthermore, these stationary states are, from a zeroth-order viewpoint, a linear superposition of *cis* and *trans* configurations. The existence and some unusual properties (such as microsecond lifetimes) of stationary eigenstates of this kind in large polyatomic molecules were examined experimentally as early as 1977^{18,19}.

The questions then arise as to how to extract and understand the quantum yield in the case of incoherent light excitation, and how to describe the *cis-trans* isomerization of retinal from a stationary eigenstate viewpoint that is appropriate for vision under natural light conditions. A substantial step towards this major goal is provided in this paper.

Here, we address this issue by first generalizing the concept of the quantum yield to the case of incoherent light excitation of a polyatomic molecule. We note that in the limit of rapid decoherence of initial coherences in the reduced density matrix, the photoreaction quantum yield is stationary. This definition is then applied to calculate the quantum yield of *cis-trans* photoisomerization of retinal using a minimal two-state, two-mode model⁴. We find excellent overall agreement between our calculated quantum yield and the previous time-dependent result of Stock and Hahn⁴. In addition, our calculations, in both the presence and absence of relaxation, agree with the observed value of the quantum yield at 500 nm and qualitatively reproduce its observed decline with increasing excitation wavelength¹¹. These findings demonstrate the role of localization properties of the stationary states in determining the quantum yields, a crucial feature in the process induced with natural light.

Note that there are various definitions of the quantum yield that are adopted in time-dependent studies. Below, we consistently utilize the parameters and approach of Ref. 4, which has become something of a “standard model” for basic retinal dynamics. This imposes a number of consistency requirements that are discussed in Sect. V.

Before proceeding further, we emphasize that incoherent excitation of biomolecules embedded in condensed-phase environments involves two processes that occur simultaneously: (a) the creation of the stationary states by the incoherent light, and (b) the relaxation between the stationary states caused by the interaction with the environment. In this work, we treat these processes sequentially, assuming that the stationary states are formed first and then relax due to the system-environment coupling. This allows for a better assessment of their individual roles. The eigenstates formed on stage (a) are considered in Secs. II and III; the effects of relaxation are considered in Sec. IV and, significantly, shown to have a negligible effect on the quantum yield of retinal photoisomerization treated within in the two-state, two-mode model⁴. The results, as

seen below, motivate a future study of simultaneous incoherent excitation and relaxation in this and related model retinal systems.

II. THE QUANTUM YIELD

We extract the quantum yield for the stationary case from the standard time dependent result, hence exposing their relationship. Reference 4 defines the photoreaction quantum yield from the time-dependent view as

$$Y = \frac{P_{\text{trans}}^{(1)}(t)}{P_{\text{cis}}^{(0)}(t) + P_{\text{trans}}^{(1)}(t)} \quad (t \rightarrow \infty), \quad (1)$$

where the time-dependent populations of 11-*cis* and all-*trans* isomers are defined as^{4,6,7}

$$P_{\alpha}^{(n)}(t) = \text{Tr}\{\rho(t)\hat{P}_{\alpha}^{(n)}\}. \quad (2)$$

Here $\rho(t)$ is the reduced density matrix of the retinal subsystem, $\alpha = 11\text{-cis}$ or $\alpha = \text{all-trans}$, and

$$\begin{aligned} \hat{P}_{\text{cis}}^{(0)} &= \Theta(\pi/2 - |\phi|)|\psi_0\rangle\langle\psi_0| \\ \hat{P}_{\text{trans}}^{(1)} &= \Theta(|\phi| - \pi/2)|\psi_1\rangle\langle\psi_1|. \end{aligned} \quad (3)$$

are the projection operators, which divide the full range of the isomerization coordinate $\phi \in [-\pi/2, 3\pi/2]$ into the *cis* ($\phi \in [-\pi/2, \pi/2]$) and *trans* regions ($\phi \in [\pi/2, 3\pi/2]$), as illustrated in Fig. 1. In Eq. (2), $\Theta(x)$ is the Heaviside step function, and the operators $|\psi_n\rangle\langle\psi_n|$ project onto the ground and excited diabatic electronic states $|\psi_0\rangle$ and $|\psi_1\rangle$. Qualitatively, $P_{\text{cis}}^{(0)}$ can be thought of as projecting onto the adiabatic ground state reactant *cis* region and $P_{\text{trans}}^{(1)}$ onto the adiabatic ground state product *trans*. In this definition, the adiabatic excited state populations $P_{\text{cis}}^{(1)}$ and $P_{\text{trans}}^{(0)}$ are neglected assuming that these populations have decayed to zero in the long-time limit. Alternative definitions [e.g., including $P_{\text{cis}}^{(1)}$ in the numerator and $P_{\text{trans}}^{(0)}$ in the denominator of Eq. (1)] are certainly possible and will be explored in future work³⁶, and would necessitate a refitting of the potential parameters to the new definition of the time-dependent quantum yield.

As an example, consider impulsive FC excitation of retinal from its ground electronic and vibrational states to the first excited electronic state $|\psi_1\rangle$. Here the density matrix of the system at time zero is given by^{4,6,8}

$$\rho(t=0) = |\psi_1\rangle|00\rangle\langle 00|\langle\psi_1| \quad (4)$$

where $|00\rangle = |n_{\phi} = 0, n_x = 0\rangle$ is the ground state with zero quanta in the torsional and coupling modes n_{ϕ} and n_x .

It is convenient to express the density matrix in the system eigenstate basis defined by $\hat{H}_S|i\rangle = \epsilon_i|i\rangle$ where ϵ_i and $|i\rangle$ are time-independent eigenvalues and eigenfunctions. In this basis, with frequencies $\omega_{ij} = (\epsilon_i - \epsilon_j)/\hbar$, $\rho_{ij}(t) = \rho_{ij}(0)e^{-i\omega_{ij}t}$. Hence the population dynamics is given by

$$P_\alpha^{(n)}(t) = \sum_{i,j} e^{-i\omega_{ij}t} \langle i|\rho(0)|j\rangle \langle j|\hat{P}_\alpha^{(n)}|i\rangle \quad (5)$$

Since the time-dependence arises from the oscillatory behavior of the coherences, (i.e., terms with $i \neq j$), if $\langle i|\rho(0)|j\rangle = 0$ then the state populations are time independent. An important example of such a case is molecular excitation with incoherent light [Eq. (5)], which populates, after some time, the eigenstates of \hat{H}_S without any subsequent coherent dynamics¹⁶. Similarly, environmentally induced effects cause the loss of coherences. In this case, retaining only the diagonal terms in Eq. (5), we have

$$P_\alpha^{(n)} = \sum_i \langle i|\rho(0)|i\rangle \langle i|\hat{P}_\alpha^{(n)}|i\rangle \quad (6)$$

This expression may be made more physically transparent by noting that the diagonal elements of the reduced density matrix following impulsive FC excitation at $t = 0$ correspond to the linear absorption spectrum of the molecule described by the spectral lineshape function²⁰ $A(\omega_i)$, where $\omega_i = (\epsilon_i - \epsilon_0)/\hbar$ is the excitation frequency measured from the ground vibrational state of the *cis*-isomer with energy ϵ_0 (we assume that this is the only vibrational state populated prior to excitation). Then it follows from Eq. (4) that

$$\langle i|\rho(0)|i\rangle = \langle i|\psi_1|00\rangle \langle 00|\langle \psi_1|i\rangle = |\langle i|\hat{\mu}|\psi_0\rangle|00\rangle|^2 = A(\omega_i) \quad (7)$$

where $\hat{\mu} = \mu_{10}|\psi_1\rangle\langle \psi_0|$ is the transition dipole moment operator, and we set $\mu_{10} = 1$ a.u. without loss of generality [since the $|\mu_{10}|^2$ prefactors multiplying state populations cancel out in the expression for Y in Eq. (1)]. Therefore, Eq. (6) may be rewritten in the form

$$P_\alpha^{(n)} = \sum_i A(\omega_i) \langle i|\hat{P}_\alpha^{(n)}|i\rangle \quad (8)$$

Hence, as expected, only the eigenvalues ϵ_i that have non-negligible probability of being excited by incoherent light make a contribution to the stationary populations in Eq. (8).

Given Eq. (8), the time-dependent definition of the quantum yield (1) extends to the frequency domain by defining

$$Y_1 = \frac{P_{\text{trans}}^{(1)}}{P_{\text{cis}}^{(0)} + P_{\text{trans}}^{(1)}} \quad (9)$$

with the “pre-averaged” populations $P_\alpha^{(n)}$ given by Eq. (8). Alternatively, we can first define a frequency-dependent *trans* / *cis* probability ratio

$$Y(\omega_i) = \frac{P_{\text{trans}}^{(1)}(\omega_i)}{P_{\text{cis}}^{(0)}(\omega_i) + P_{\text{trans}}^{(1)}(\omega_i)}, \quad (10)$$

where $P_\alpha^{(n)}(\omega_i) = \langle i | \hat{P}_\alpha^{(n)} | i \rangle$ are the expectation values of the projection operators in Eq. (8). The resulting frequency-dependent quantum yield (10) can be averaged with the normalized spectral line shape function to give

$$Y_2 = \sum_i A(\omega_i) Y(\omega_i) \quad (11)$$

It is clear that the definitions (9) and (11), termed the “pre-averaged” and “post-averaged” quantum yield, are not equivalent, but both provide a physically meaningful measure of (frequency-dependent) photoreaction efficiency. Specifically, the pre-averaged definition (9) is consistent with the original definition of Hahn and Stock [Eq. (1)]⁴, whereas the post-averaged definition admits a clear physical interpretation as the degree of *cis* vs. *trans* character of a collection of eigenstates independently excited by incoherent light. Expressions related to Eqs. (9) and (11) were previously obtained in References 21 and 22, where the long-time limits of electronic state populations were associated with the phase volumes occupied by the wavepackets evolving on the upper and lower adiabatic potential energy surfaces.

Equations (5), (8), (9), and (11) form the central tool for the computations below. They generalize the quantum yield in Eq. (1) to the frequency domain relevant to stationary eigenstates, and provide a theoretical basis for the computational study of photoinduced isomerization in model retinal as described below. The essential physics comes from the recognition that the established time dependent definition [Eq. (1)] relies entirely on the projections onto domains of ϕ to define *cis* vs. *trans* configurations. Indeed, each of Eqs. (1), (9) and (11) have essentially the same meaning, the fraction of population in the ground adiabatic state that is, in the long time limit, in the *trans*-configuration, disregarding any initial population in ground-state *cis* well. This is achieved in Eq. (1) by placing all population in an initial wavepacket on the excited electronic surface. Equations (9) and (10) achieve this by putting all population initially into a stationary mixture on the excited potential surface. What the latter two equations emphasize is that in the presence of incoherent light and decoherence, the appropriate states to consider in the long time limit are the stationary eigenstates of the Hamiltonian. They, as seen below, will allow stationary state insight into the efficiency of the isomerization process.

Below, we apply this formulation to evaluate the quantum yield for the primary photoreaction in rhodopsin using the two-state two-mode model²³, which was previously applied⁴ to linear absorption⁵, Raman⁵, and femtosecond pump-probe⁷ spectra of retinal in rhodopsin. The two-state two-mode model and its multidimensional (25-mode) extension⁵ have since been used to explore quantum dynamics and coherent control of *cis-trans* photoisomerization of retinal chromophore in rhodopsin²⁴⁻²⁶. We note that the model has the following advantages over the one-dimensional scenario (e.g. Ref. 30): (1) the present model is two-dimensional, including a relevant bend degree of freedom; (2) it accounts for the conical intersection between the ground and the first excited electronic states of retinal; (3) it reproduces many salient features of the experimentally measured isomerization dynamics, including the ultrafast 200 fs timescale, the transient pump-probe spectra, and the energy storage of the photoreaction.

III. COMPUTATIONAL RESULTS

We emphasize that the two-state two-mode model and the associated definition of the quantum yield [Eq. (1)] were previously parametrized so as to reproduce various properties of the photoreaction⁵ of retinal in rhodopsin. It neglects the effects of solvation, which are known to dramatically affect the photoisomerization dynamics in solution³⁷⁻³⁹, but does include, due to the parameter fit, some features of the interaction of the two modes with the remaining molecular background. Our study is thus restricted to *cis-trans* photoisomerisation of retinal in rhodopsin.

The wavefunctions $|i\rangle$ in Eq. (8) are the eigenfunctions of the 2D model Hamiltonian given by^{4,6,23}

$$H_S = T\delta_{nn'} + \begin{pmatrix} E_0 + \frac{1}{2}\tilde{V}_0(1 - \cos\phi) + \frac{\omega}{2}x^2 & \lambda x \\ \lambda x & E_1 - \frac{1}{2}\tilde{V}_1(1 - \cos\phi) + \frac{\omega}{2}x^2 + \kappa x \end{pmatrix}. \quad (12)$$

where $T = -\frac{1}{2m}\frac{\partial^2}{\partial\phi^2} + \frac{\omega}{2}\frac{\partial^2}{\partial x^2}$ is the kinetic energy operator, ϕ is the tuning mode (or generalized reaction coordinate) corresponding to low-frequency torsional modes, and x is the coupling mode that corresponds to high-frequency unreactive modes. The second term on the right-hand side of Eq. (12) is the interaction potential in a basis spanned by the diabatic electronic functions $|\psi_n\rangle$ with $n = 0, 1$ ⁴. A plot of the adiabatic PESs obtained by diagonalizing the potential energy term in Eq. (12) is shown in Fig. 1. The model parameters E_n , \tilde{V}_n , ω , κ , and λ , chosen to reproduce the femtosecond dynamics of retinal in rhodopsin^{4,6}, are (in eV): $E_0 = 0$, $E_1 = 2.48$, $\tilde{V}_0 = 3.6$, $\tilde{V}_1 = 1.09$, $\omega = 0.19$, $\kappa = 0.1$, $\lambda = 0.19$, and $m^{-1} = 4.84 \times 10^{-4}$.

A total of 900 eigenvalues and eigenvectors of \hat{H}_S were calculated and used to assemble the matrix elements of the projector operators and the lineshape function in Eqs. (9) and (11). The converged $A(\omega)$ was in agreement with results in Ref. 4. Interestingly, we found that the spectrum could be classified as integrable, insofar as the nearest neighbor distribution of energy levels $\Delta\epsilon$ shows a structure that can be fit with a Poisson distribution $P(S) = D^{-1} \exp(-S/D)$ with the local mean spacing $D = 24.081 \text{ cm}^{-1}$ (see, e.g., Ref. 27). Such distributions are becoming of increasing interest due, e.g. to a recent proposal²⁸ regarding chaos and transport in biological processes.

The upper panel of Figure 1 shows torsional profiles of the adiabatic potential energy surfaces (PES) obtained by diagonalizing the Hamiltonian matrix (12) at $x = 0$. The PES profiles exhibit a conical intersection at $\phi \approx \pi/2$ and $x = 0$, clearly visible in the two-dimensional plot in the lower panel of Fig 1. The *cis* isomer of retinal is localized in the potential well of the lower diabatic PES ($n = 0$) on the left-hand side. Photoexcitation by incoherent light (represented by a green arrow) populates a number of stationary eigenstates (grey lines) with mixed *cis-trans* character. The quantum yield is determined by projecting these eigenstates onto their respective *cis* and *trans* regions of configuration space as discussed above.

Figure 2 shows the frequency-dependent quantum yield $Y(\omega_i)$ given by Eq. (10) as a function of excitation energy (measured from the ground vibrational state of *cis*-isomer). Here [from Eq. (10)], pure *cis* states correspond to $Y = 0$ and pure *trans* states correspond to $Y = 1$; thus, the magnitude of $Y(\omega_i)$ reflects the *cis* or *trans* character of a particular eigenstate with energy $\epsilon_i = \hbar\omega_i$. As expected, all molecular eigenstates that occur below the minimum energy of the *trans* well ($11,000 \text{ cm}^{-1}$, see Fig. 2) have negligible quantum yields due to the absence of *trans* eigenstates in this low energy range. Above the $11,000 \text{ cm}^{-1}$ threshold, the quantum yield is a rapidly varying irregular function of ω_i , reflecting the strong mixing between the *cis* and *trans* components by the full Hamiltonian. Such mixed *cis-trans* eigenstates are conceptually similar to the long-lived eigenstates of mixed singlet-triplet character observed in pentacene^{18,19}.

Interestingly, a closer inspection of Fig. 2, as shown in the figure insert, reveals the presence of purely *cis* (or *trans*) eigenstates with $Y(\omega_i) = 0$ (or 1), which are qualitatively similar to the electronically localized eigenstates in vibronically coupled systems such as pyrazine³². The effect has recently been analyzed in the context of geometric phase-induced localization^{33,34}. However, such “extreme states” may well be a result of low dimensionality of the model, as is indeed the case in pyrazine³⁵.

Table I lists the values of the quantum yield computed using the stationary eigenstates of the 2D model (the corresponding $A_{2D}(\omega)$ is shown by the green line in Fig. 2)^{4,6}. Both pre-averaged and post-averaged results ($Y_1 = 0.63$ and $Y_2 = 0.62$) agree extremely well with the previous time-dependent wavepacket result⁴ of $Y_{TD} = 0.63$. The fact that the stationary quantum yields agree so well with time-dependent calculations^{4,6} makes clear how the quantum yield is directly manifest in the stationary eigenstates. Moreover, we also note agreement with the measured value¹¹ of 0.65 ± 0.01 . The agreement with experiment is a natural consequence of the two-state two-mode model⁴ being parametrized to reproduce the measured quantum yield in time-dependent calculations.

In order to explore the effect of $A(\omega)$ on the calculated quantum yields, we replaced the 2D model lineshape function in Eqs. (9) and (11) by the experimentally measured absorption profile of retinal in rhodopsin¹¹ shown by the red line in Fig. 2. The result gives $Y = 0.43$, in worse agreement with experiment than the value obtained with $A_{2D}(\omega)$. This confirms that the potential surfaces are optimized for behavior in the domain shown in green in Fig. 2, but would require further work to properly represent the *cis/trans* branching in other energy regions.

Mathies and co-workers¹¹ also measured $Y(\omega)$ observing a decline in the photoreaction efficiency below 500 nm. For comparison, we calculate the wavelength-resolved stationary quantum yields by dividing the entire λ interval into 10 nm-wide bins, and average Eqs. (9) and (11) over the eigenstates with energies falling into a particular bin. As with the overall quantum yield, two related, but not identical, definitions are possible. In the first, one calculates the averaged *cis* and *trans* populations

$$\bar{P}_\alpha^{(n)}(\omega_i) = \sum_{j \in i\text{-th bin}} P_\alpha^{(n)}(\omega_j) A(\omega_j) \quad (13)$$

where $\omega_i = 2\pi c/\lambda_i$ is the center frequency corresponding to i -th bin, and define:

$$Y_1(\omega_i) = \frac{\bar{P}_{\text{trans}}^{(1)}(\omega_i)}{\bar{P}_{\text{trans}}^{(1)}(\omega_i) + \bar{P}_{\text{cis}}^{(0)}(\omega_i)} \quad (14)$$

As an alternative, we directly average the frequency-dependent quantum yield (11) over the entire bin

$$Y_2(\lambda_i) = Y_2 \left(\frac{2\pi c}{\omega_i} \right) = N_i^{-1} \sum_{j \in i\text{-th bin}} Y(\omega_j) A(\omega_j) \quad (15)$$

where $N_i = \sum_{j \in i\text{-th bin}} A(\omega_j)$ is a normalization factor that serves to correct for the change in absorption intensity due to the varying λ .

Figure 3 compares the wavelength dependent quantum yield with the experimental results in the 500-570 nm range (Ref. 11). While the observed quantum yield declines monotonically with

λ and stays constant below $\lambda = 500$ nm, our theoretical values oscillate over the entire range of λ . Above 500 nm, the calculated quantum yields tend to decline with λ , in qualitative agreement with experiment (the only exception being the value of Y_2 at 540 nm). As expected from the above analysis (see Table I), switching lineshape functions has a dramatic effect on the calculated quantum yields. In contrast with the results presented in Table I, however, using the experimental $A(\omega)$ improves the overall agreement with experiment, particularly at $\lambda > 500$ nm.

Also shown in the inset of Fig. 3 is the “bare” frequency-dependent quantum yield,

$$Y_{\text{av}}(\lambda_i) = N_i^{-1} \sum_{j \in i\text{-th bin}} Y(\omega_j). \quad (16)$$

Here, the absence of the spectral lineshape function [present in Eqs. (9) and (11)] reveals the variation in *cis* / *trans* character of molecular eigenstates with zero oscillator strengths, which do not contribute to the physical quantum yield (15). The $Y_{\text{av}}(\lambda)$ [inset of Fig. 3] is seen to generally decline with increasing λ . This behavior reflects the appearance of *trans* states at energies above $11,000 \text{ cm}^{-1}$, and that their density in this region is smaller than that of *cis* states (see Fig. 2). Thus, the *trans* character of molecular eigenstates can be expected to decrease with decreasing ω_i , as is implicit in the experimental results. While the downward trend in the wavelength dependence of Y_{av} (inset of Fig. 3) is somewhat more pronounced than that observed for Y_1 and Y_2 (Fig. 3), we note that the former cannot be directly compared with experiment. This is because the bare quantum yield [Eq. (16)] does not include the variation of the spectral lineshape function $A(\omega)$ with ω .

IV. EFFECTS OF RELAXATION ON QUANTUM YIELD

Our computed time-independent definitions of the quantum yield [Eq. (9) and (11)] assume that the eigenstate populations ρ_{ii} do not depend on time. In reality, however, the populated eigenstates undergo relaxation due to the interaction with the environment. To elucidate the effect of the relaxation on the quantum yield, we calculated the transition rates $W_{j \leftarrow i}$ between eigenstates $|i\rangle$ and $|j\rangle$ using Fermi’s Golden Rule⁴¹

$$W_{j \leftarrow i} = \sum_{\gamma=\phi,x} |\langle i | \hat{Q}_\gamma | j \rangle|^2 (1 + N(|\omega_{ji}|)) J_\gamma(|\omega_{ji}|) \quad (\omega_{ji} < 0) \quad (17)$$

and

$$W_{j \leftarrow i} = \sum_{\gamma=\phi,x} |\langle i | \hat{Q}_\gamma | j \rangle|^2 N(\omega_{ji}) J_\gamma(\omega_{ji}) \quad (\omega_{ji} > 0), \quad (18)$$

where $N(\omega) = [\exp(\hbar\omega/kT) - 1]^{-1}$ is the Bose distribution at temperature $T = 300$ K, k is the Boltzmann's constant, and $J_\gamma(\omega) = \eta_\gamma e^{-\omega_\gamma/\omega_{c\gamma}}$ is the spectral density of the bath modes representing low-frequency, non-reactive vibrational modes⁵ coupled to degree of freedom $\gamma = \phi, x$. Following Stock and co-workers⁶, we adopt an Ohmic spectral density $J(\omega) = \eta_\gamma e^{-\omega/\omega_{c\gamma}}$ with $\eta_\phi = 0.15$, $\omega_{c\phi} = 0.08$ eV, $\eta_x = 0.1$, and $\omega_{cx} = 0.19$ eV. The bath operators \hat{Q}_γ in Eqs. (17)-(18) are given by⁸ $\hat{Q}_\phi = (1 - \cos \phi)|\psi_1\rangle\langle\psi_1|$ and $\hat{Q}_x = x|\psi_1\rangle\langle\psi_1|$.

Figure 4(a) shows the time dependence of the expectation values $P_{\text{cis}}^{(n)}(t)$ and $P_{\text{trans}}^{(n)}(t)$ in Eq. (2) obtained by propagating the rate equations parametrized by the transition rates given by Eqs. (17)-(18) with the initial condition $\rho_{ij}(t = 0) = \delta_{ij}A(\omega_i)$, *i.e.* assuming fully incoherent excitation with natural light. A substantial fraction of population at $t = 0$ resides in the excited diabatic electronic states [$P_{\text{cis}}^{(1)} + P_{\text{trans}}^{(1)} = 0.69$]. The interaction with low-frequency bath modes leads to dissipation of the electronic and vibrational energy, manifested in the decay of the excited-state populations $P_{\text{cis}}^{(1)}(t)$ and $P_{\text{trans}}^{(0)}(t)$. The decay is accompanied by a growth of the ground-state populations $P_{\text{cis}}^{(0)}(t)$ and $P_{\text{trans}}^{(1)}(t)$ shown by the solid lines in Fig. 4(a).

Figure 4(b) plots the time dependence of the quantum yield given by Eq. (1). Remarkably, the quantum yield shows only a weak time dependence, with deviations from the asymptotic value of 0.62 not exceeding 3% over the time interval studied (0 – 3 ps). Thus, while the individual *cis* and *trans*-populations evolve in time, the value of the quantum yield, defined as their ratio via Eq. (9), remains constant.

Analysis of the system-bath coupling matrix elements [Eq. (17)] shows that the matrix elements involving the torsional degree of freedom ϕ are small compared to those of the coupling mode x . We can therefore expect that relaxation of the initial “bright” eigenstates populated by incoherent FC excitation (see below and Fig. 5) is driven by the interaction of the coupling mode with the bath oscillators. Indeed, as shown in Fig. 4(b), neglecting the ϕ -component of the system-bath coupling (dashed curve) has little effect on the time variation of the quantum yield. The dominant role played by the coupling mode in the relaxation process is at the heart of our arguments presented below that analyze the lack of time dependence of the quantum yield.

In order to gain insight into relaxation dynamics, we plot in Fig. 5 the transient linear absorption spectrum of the two-state, two-mode model [e.g. the populations $\rho_{ii}(t)$] during the various stages of the relaxation process. At time zero, an incoherent mixture of “bright” eigenstates is assumed to follow FC excitation from the ground state. The three dominant “bright” eigenstates that account for over 40% of all $t = 0$ excited-state population are $|512\rangle$, $|507\rangle$, and $|508\rangle$, and are focused upon

below. As time proceeds, the eigenstates begin to relax due to the interaction with the phonon bath. At $t = 100$ fs, the population is seen to be spread over three lower-lying manifolds of states, which are separated from the initial “bright” manifold by a constant energy gap. The dominant eigenstates populated in the decay of the bright state $|512\rangle$, are shown in Fig. 6. We observe that during the course of relaxation, the population “branches out” into different final eigenstates until it finally settles in a steady state characterized by a stationary eigenstate distribution shown in the lowermost panel of Fig. 5. The steady state defines the asymptotic ($t \rightarrow \infty$) limit of the quantum yield, and is thus of particular importance to the theoretical description.

According to Fermi’s Golden Rule (17), the relaxation rates are determined by (a) the magnitude of the system-bath coupling matrix element, and (b) the value of the spectral density at the transition frequency $J(\omega_{ij})$. The existence of multiple intermediate relaxation stages in Fig. 6 is a consequence of a fixed cutoff frequency of the bath $\omega_{cx} = 0.19$ eV. Because the Ohmic spectral density function peaks at $\omega = \omega_{cx}$ and decays quickly away from the maximum⁴², relaxation to the eigenstates separated from the initial state by the energy window $\hbar\omega_{cx} \pm \hbar\Delta\omega$ is allowed (provided that the corresponding coupling matrix elements are non-zero), whereas relaxation to the eigenstates outside the energy window cannot occur via single phonon-emission. However, such lower-lying eigenstates are populated via multiple phonon emission (or relaxation cascade), as illustrated in Fig. 6.

As for the quantum yield, relaxation influences the quantum yield through the time dependence of the populations $\rho_{ii}(t)$ which changes the eigenstates that contribute to the evolving quantity:

$$Y_1(t) = \frac{\sum_i \rho_{ii}(t) \langle i | \hat{P}_{\text{trans}}^{(1)} | i \rangle}{\sum_i \rho_{ii}(t) \langle i | \hat{P}_{\text{cis}}^{(0)} | i \rangle + \sum_i \rho_{ii}(t) \langle i | \hat{P}_{\text{trans}}^{(1)} | i \rangle} \quad (19)$$

Therefore, in order to understand the time dependence of the quantum yield, it is necessary to follow both the time evolution of the populations $\rho_{ii}(t)$ and their localization properties, as manifest in the matrix elements of $\hat{P}_{\text{cis}}^{(0)}$ and $\hat{P}_{\text{trans}}^{(1)}$. To examine the localization, we define the probability density $P_i^{(n)}(\phi, x)$ for eigenstate $|i\rangle$ projected onto the diabatic electronic state $n = 0, 1$

$$P_i^{(n)}(\phi, x) = \int d\mathbf{r}_e |\psi_i^{(n)}(\phi, x; \mathbf{r}_e)|^2, \quad (20)$$

where $\psi_i^{(n)}(\phi, x; \mathbf{r}_e)$ are the diabatic components of the eigenstate $|i\rangle$ described by the wavefunction

$$\psi_i(\phi, x; \mathbf{r}_e) = \sum_{n=0,1} \psi_i^{(n)}(\phi, x; \mathbf{r}_e) = \sum_{n=0,1} \sum_{\mu,\nu} C_{n\mu\nu} \Phi_\mu^{(n)}(\phi) X_\nu^{(n)}(x) \psi_n(\mathbf{r}_e), \quad (21)$$

where the direct-product basis $\Phi_{\mu}^{(n)}(\phi)X_{\nu}^{(n)}(x)$ is chosen in such a way as to diagonalize the torsional vibronic coupling Hamiltonian (12) at $\lambda = 0$ (no vibronic coupling). In this latter case, the problem reduces to that of two non-interacting electronic states, and the eigenstates (21) factorize into products of basis functions that depend on the ϕ and x coordinates

$$\psi_i(\phi, x; \mathbf{r}_e) = \Phi_{\mu}^{(n)}(\phi)X_{\nu}^{(n)}(x)\psi_n(\mathbf{r}_e), \quad (22)$$

This expression for the system eigenstates provides a reasonable zeroth-order approximation to the true eigenstates of the vibronic coupling Hamiltonian (12) in the energy region below the conical intersection ($\epsilon < 14,000 \text{ cm}^{-1}$)³⁶. Here, the low-lying eigenstates of the full vibronic Hamiltonian are localized in their own potential wells^{33,34} (as clearly observed in Fig. 2). However, as the energy increases above the conical intersection, the eigenstates become strongly mixed by the vibronic coupling, and delocalize over the whole configuration space.

An example of such behavior is shown in Fig. 7, which shows the probability density of the bright eigenstate $|512\rangle$ together with that of the ground state $|1\rangle$ and the eigenstates populated in the first few relaxation stages (green arrows in Fig. 6). The bright state has a large probability amplitude in the *cis*-region of the first excited diabatic state, which maximizes its overlap with the ground *cis*-state, to enhance excitation. The lower-lying states $|419\rangle$ and $|423\rangle$ start to experience the repulsive wall of the $n = 1$ diabatic potential in the *cis*-region of configuration space (see Fig. 1). As a result, the population is completely transferred away from the repulsive region to the ground *cis* and excited *trans* regions. There is no apparent preference for either *cis* or *trans* regions during these initial relaxation stages due to the strong mixing of all degree of freedom: As shown in Fig. 4(a), both $P_{\text{cis}}^{(0)}$ and $P_{\text{trans}}^{(1)}$ increase monotonically with time.

After being transferred one step below below the initial state, the population continues to relax to lower-lying eigenstates while preserving its profile along the reaction coordinate. This can be attributed to the particular form of the system-bath coupling, which primarily depends on the x coordinate and hence does not strongly alter the ϕ -profiles of the eigenstates coupled by the bath. In particular, we verified that the amount of *cis* and *trans* character of most of the states involved in the relaxation process is approximately constant. Exceptions do occur because of the strong vibronic coupling, which may occasionally change the ϕ distribution of some eigenstates due to the coupling mediated by the x coordinate. However, this situation is an exception rather than the rule: As shown in Fig. 8, only two out of ~ 20 eigenstates involved in the first stage of relaxation ($|421\rangle$ and $|415\rangle$) are dramatically different in their *trans*-character (as quantified by the matrix

element $\langle i | \hat{P}_{\text{trans}}^{(1)} | i \rangle$) from the other states. As a result, the quantum yield varies only weakly with time.

A dramatic change in the relaxation mechanism occurs when the eigenstate energy falls below that of the conical intersection. Figure 9 shows that the eigenstates to which relaxation then occurs become localized in their corresponding *cis*- and *trans*- wells. The population of the initial (delocalized) eigenstate $|346\rangle$ relaxes to two eigenstates, one of which ($|279\rangle$) is strongly localized in the *trans*-well and the other ($|281\rangle$) has more probability amplitude in the *cis*-well (see Supplementary Material⁴³). As the population gets partitioned between the two eigenstates, the quantum yield remains unaltered again due to the ϕ -independent nature of the system-bath coupling, which tends to conserve the angular probability density of all eigenstates involved.

Finally, we consider the final stages of the relaxation process depicted in Fig. 9. These represent bath-induced transitions between localized eigenstates, and can be understood by noting that the eigenstates are given to zeroth order by Eq. (22). For simplicity, let us assume that the value of the quantum yield before relaxation begins is determined by a single eigenstate α . After relaxation is over, the population is transferred to the eigenstate $|\alpha'\rangle$. Taking the matrix elements of $\hat{P}_{\text{trans}}^{(1)}$ and using Eq. (22), we find

$$\langle \alpha | \hat{P}_{\text{trans}}^{(1)} | \alpha \rangle = \langle \Phi_{\mu}^{(1)}(\phi) X_{\nu}^{(1)}(x) | \hat{P}_{\text{trans}}^{(1)} | \Phi_{\mu}^{(1)}(\phi) X_{\nu}^{(1)}(x) \rangle = \langle \Phi_{\mu}^{(1)}(\phi) | \hat{P}_{\text{trans}}^{(1)} | \Phi_{\mu}^{(1)}(\phi) \rangle \quad (23)$$

because $\hat{P}_{\text{trans}}^{(1)}$ does not depend on x , and similarly

$$\langle \alpha' | \hat{P}_{\text{trans}}^{(1)} | \alpha' \rangle = \langle \Phi_{\mu'}^{(1)}(\phi) | \hat{P}_{\text{trans}}^{(1)} | \Phi_{\mu'}^{(1)}(\phi) \rangle. \quad (24)$$

But the system-bath coupling operator does not depend on ϕ , and hence cannot change the number of quanta in the torsional mode μ , so the right-hand sides of Eqs. (23) and (24) are equal.

This result suggests that in the low-energy regime of localized eigenstates, the quantum yield of *any* process that depends on a single reaction coordinate should be time-independent, provided that the system-bath coupling does not depend on that coordinate. This is clearly illustrated in Fig. 9: the localized state $|279\rangle$ has 3 peaks along the x coordinate, corresponding to 2 quanta in the x -mode ($\nu = 2$). The system-bath coupling changes ν from 2 to 1 and then from 1 to 0, while leaving the ϕ distribution unchanged (see also Figs. 1 and 2 of Supplementary Material⁴³). The final eigenstate $|171\rangle$ is vibrationally “cold” with respect to the coupling mode, but remains highly excited along the torsional coordinate.

A few closing remarks are in order concerning the asymptotic ($t \rightarrow \infty$) value of the quantum yield that corresponds to the population distribution shown in the lowermost panel in Fig. 6. The

steady state is obtained by propagating the rate equations of motion for the populations, which is a numerically efficient procedure that scales quadratically with the number of eigenstates⁴¹. The nature of the steady state is determined by the form of the system-bath coupling, and the initial conditions. We emphasize that this steady-state solution does *not* have the form of the Boltzmann distribution that would be normally expected of Pauli-type rate equations in the limit $t \rightarrow \infty$ ⁴⁴. Rather, in accord with Ref. 45, our steady-state distribution corresponds to a metastable state, which will eventually tunnel to the *cis*-well (at least if the well is one-dimensional). The large barrier height in the two-state two-mode model makes the tunneling timescale extremely long compared to any other timescale of interest in this system. As a possible direction of future research, it would be interesting to explore whether such metastable steady states can be obtained without propagating the dynamical equations of motion. If so, the determination of the quantum yield from the stationary eigenstates becomes a straightforward task via Eq. (9) with the matrix elements ρ_{ii} replaced by their steady-state values.

V. SUMMARY AND DISCUSSION

We have considered a time-independent approach to the quantum yield of *cis-trans* photoisomerization, here applied to model retinal in rhodopsin. The need for this approach arises due to the recognition that natural processes take place in incoherent light (e.g., sunlight with a coherence time of 1.32 fs) and environmental decoherence, which produce mixtures of stationary Hamiltonian eigenstates. Here we have recast one of the standard time-dependent definitions of the quantum yield in terms of time-independent quantities, the eigenstates of the Hamiltonian and associated dipole transition matrix elements. The quantum yield is then shown to be a direct reflection of the *cis* vs. *trans* character of the individual stationary eigenstates of the system and the associated dipole transition matrix elements from the ground electronic state. Further, applied to a model of retinal, this approach gives excellent results for the quantum yield, fully in agreement with experiment. Interestingly, relaxation from the initially prepared stationary mixture does not alter the quantum yield, a consequence of both the *cis/trans* partitioning of the stationary states and the system-bath coupling in this well established minimalist model of retinal isomerization.

Ideally, we should consider a full treatment of all modes of retinal in a proper rhodopsin environment, define the quantum yield and other observable properties, fit the retinal potential parameters to experiment, and compare time-dependent computational results to the stationary state

results associated with incoherent light excitation. However, such an extensive computational study is not required to support the main result of this paper, i.e., that the stationary eigenstates of the system Hamiltonian provide an alternative and important way to understand features affecting the quantum yield in incoherent light. Rather, we adopt the basic two-dimensional model of Hahn and Stock^{4,5}. Restricting attention to this model necessitates, by requirements of consistency, that if we adopt their two-dimensional potentials and associated system parameter fits to experimental data, that we also must maintain their definition of quantum yield, with the associated neglect of $P_{\text{cis}}^{(1)}(t)$ and $P_{\text{trans}}^{(0)}(t)$. Alternative definitions of the quantum yield would have resulted in different values of the system parameter fits and different stationary eigenstates of the Hamiltonian. Hence, the successful computational results demonstrated here do motivate a more extensive calculation of retinal Hamiltonian eigenstates for a retinal model including all degrees of freedom²⁶. Such work is in progress.

Acknowledgments. This work was supported by the Natural Sciences and Engineering Research Council of Canada, and by the US Air Force Office of Scientific Research under contract numbers FA9550-10-1-0260 and FA9550-13-1-0005.

Table I. Calculated quantum yields for retinal photoisomerization. Both pre-averaged (Y_1) and post-averaged (Y_2) results are shown. $A_{2D}(\omega)$ – normalized lineshape function calculated within the 2D model; $A_{exp}(\omega)$ – normalized lineshape function based on the measured absorption spectrum of retinal in rhodopsin¹¹. The time-dependent wavepacket result from Ref. 4 is given in the last column.

Quantum yield	$A_{2D}(\omega)$	$A_{exp}(\omega)$	Experiment ¹¹	Time-dependent ⁴
Y_1	0.62	0.43	0.65 ± 0.01	0.63
Y_2	0.63	0.45		

* ttscherb@chem.utoronto.ca

- ¹ Mathies, R. A.; Lugtenburg, J. in *Handbook of Biological Physics, Volume 3: Molecular Mechanisms in Visual Transduction*, Eds. D. G. Stavenga, W. J. DeGrip and E. N. Pugh Jr., Elsevier Science Press, pp. 55-90 (2000).
- ² Wang, Q.; Schoenlein, R. W.; Peteanu, L. A.; Mathies, R. A.; Shank, C. V. Vibrationally Coherent Photochemistry in the Femtosecond Primary Event of Vision. *Science* **1994**, 266, 422-424.
- ³ Polli, D.; Altoè, P.; Weingart, O.; Spillane, K. M.; Manzoni, C.; Brida, D.; Tomasello, G.; Orlandi, G.; Kukura, P.; Mathies, R. A.; Garavelli, M.; Cerullo, G. Conical Intersection Dynamics of the Primary Photoisomerization Event in Vision. *Nature (London)* **2010**, 467, 440-443.
- ⁴ Hahn, S.; Stock, G. Quantum-Mechanical Modeling of the Femtosecond Isomerization in Rhodopsin. *J. Phys. Chem. B* **2000**, 104, 1146-1149.
- ⁵ Hahn, S.; Stock, G. Femtosecond Secondary Emission Arising from the Non-adiabatic Photoisomerization in Rhodopsin. *Chem. Phys.* **2000**, 259, 297-312.
- ⁶ Balzer, B.; Hahn S.; Stock, G. Mechanism of a Photochemical Funnel: A Dissipative Wave-Packet Dynamics Study. *Chem. Phys. Lett.* **2003**, 379, 351-358.
- ⁷ Balzer, B.; Stock, G. Transient Spectral Features of a *cis-trans* Photoreaction in the Condensed Phase: A Model Study. *J. Phys. Chem. A* **2004**, 108, 6464-6473.
- ⁸ Balzer B.; Stock, G. Modeling of Decoherence and Dissipation in Nonadiabatic Photoreactions by an Effective-scaling Nonsecular Redfield Algorithm. *Chem. Phys.* **2005**, 310, 33-41.

- ⁹ Xu, L.-J. *et al.* Spatiotemporal Manipulation of Retinoic Acid Activity in Zebrafish Hindbrain Development via Photo-isomerization. *Development* **2012**, *139*, 3355-3362.
- ¹⁰ Rieke F.; Baylor, Single Photon Detection by Rod Cells of the Retina. *Rev. Mod. Phys.* **1998**, *70*, 1027-1036.
- ¹¹ Kim, J. E.; Tauber, M. J.; Mathies, R. A. Wavelength Dependent Cis-Trans Isomerization in Vision. *Biochemistry* **2001**, *40*, 13774-13778.
- ¹² Kim, J. E.; Tauber, M. J.; Mathies, R. A. Analysis of the Mode-Specific Excited-State Energy Distribution and Wavelength-Dependent Photoreaction Quantum Yield in Rhodopsin. *Biophys. J.* **2003**, *84*, 2492-2501.
- ¹³ Sadeq, Z.; Brumer, P. Transient Quantum Coherent System Response Induced by a Partially Coherent Radiation Field. *J. Chem. Phys* **2014**, in press.
- ¹⁴ Tscherbul, T. V.; Brumer, P. Coherent dynamics of Rydberg atoms in cosmic-microwave-background radiation. *Phys. Rev. A* **2014**, *89*, 013423-1–013423-8
- ¹⁵ Grinev, T.; Brumer P. (manuscript in preparation)
- ¹⁶ Jiang, X.-P.; Brumer, P. Creation and Dynamics of Molecular States Prepared with Coherent vs Partially Coherent Pulsed Light. *J. Chem. Phys.* **1991**, *94*, 5833-5843.
- ¹⁷ Brumer, P.; Shapiro, M. Molecular Response in One-photon Absorption via Natural Thermal Light vs. Pulsed Laser Excitation. *Proc. Nat. Acad. Sci. U.S.A.* **2012**, *109*, 19575-19578.
- ¹⁸ Zewail, A. H.; Orłowski, T. E.; Jones, K. E. Radiationless Relaxation in “Large” Molecules: Experimental Evidence for Preparation of True Molecular Eigenstates and Born-Oppenheimer States by a Coherent Laser Source. *Proc. Natl. Acad. Sci. USA* **1977**, *74*, 1310-1314.
- ¹⁹ Zewail, A. H.; Jones, K. E.; Orłowski, T. E. Laser Excitation of Stationary States in Molecules: The Coupling of Real Eigenstates to Phonons and Photons. *Spectr. Lett.* **1977**, *10*, 115-125.
- ²⁰ Zare, R. N. *Angular Momentum* (Wiley, New York, 1988), pp. 136-138.
- ²¹ Manthe, U.; Köppel, H. Dynamics on potential energy surfaces with a conical intersection: Adiabatic, intermediate, and diabatic behavior. *J. Chem. Phys.* **1990**, *93*, 1658-1669.
- ²² Müller, U.; Stock, G. Flow of zero-point energy and exploration of phase space in classical simulations of quantum relaxation dynamics. II. Application to non-adiabatic processes. *J. Chem. Phys.* **1999**, *111*, 77-88.
- ²³ Seidner L.; Domcke, W. Microscopic modelling of photoisomerization and internal-conversion dynamics. *Chem. Phys.* **1994**, *186*, 27-40.

- ²⁴ Abe, M.; Ohtsuki, Y.; Fujimura, Y.; Domcke, W. Optimal Control of Ultrafast *cis-trans* Photoisomerization of Retinal in Rhodopsin via a Conical Intersection. *J. Chem. Phys.* **2005**, *123*, 144508-1-144508-10.
- ²⁵ Flores, S.-C.; Batista, V. S. Model Study of Coherent-Control of the Femtosecond Primary Event of Vision. *J. Phys. Chem. B* **2004**, *108*, 6745-6749.
- ²⁶ Arango, C.; Brumer, P. Communication: One-photon Phase Control of *cis-trans* Isomerization in Retinal. *J. Chem. Phys.* **2013**, *138*, 071104-1-071104-3.
- ²⁷ Leitner, D. M.; Köppel, H.; Cederbaum, L. S. Statistical Properties of Molecular Spectra and Molecular Dynamics: Analysis of their correspondence in NO₂ and C₂H₄⁺. *J. Chem. Phys.* **1996**, *104*, 434-443.
- ²⁸ Gabor, V.; Kauffman; Niiranen S. Quantum Biology on the Edge of Quantum Chaos. ArXiv: 1202.6433
- ²⁹ Breuer, H.-P.; Petruccione, F. *The Theory of Open Quantum Systems* (Oxford University Press, New York, 2002).
- ³⁰ Hoki, K.; Brumer, P. Excitation of Biomolecules by Coherent vs. Incoherent Light: Model Rhodopsin Photoisomerization. *Procedia Chem.* **2011**, *3*, 122-131.
- ³¹ Pachón, L. A.; Brumer, P. Incoherent excitation of thermally Equilibrated Open Quantum Systems. *Phys. Rev. A* **2013**, *87*, 022106-1-022106-10.
- ³² Sukharev, M.; Seideman, T. Optimal Control Approach to Suppression of Radiationless Transitions. *Phys. Rev. Lett.* **2004**, *93*, 093004-1-093004-4.
- ³³ Ryabinkin, I. G.; Izmaylov, A. F. Geometric Phase Effects in Dynamics Near Conical Intersections: Symmetry Breaking and Spatial Localization. *Phys. Rev. Lett.* **2013**, *111*, 220406-1-220406-4.
- ³⁴ Joubert-Doriol, L.; Ryabinkin, I. G.; Izmaylov, A. F. Geometric Phase Effects in low-energy dynamics near conical intersections: A study of the multidimensional linear vibronic coupling model. *J. Chem. Phys.* **2013**, *139*, 234103-1-234103-10.
- ³⁵ Christopher, P. S.; Shapiro, M.; Brumer, P. Overlapping Resonances in the Coherent Control of Radiationless transitions: Internal Conversion in Pyrazine. *J. Chem. Phys.* **2005**, *123*, 064313-1-064313-9.
- ³⁶ Tscherbul, T. V.; Brumer, P. (work in progress).
- ³⁷ Waddell, W. H.; Crouch, R.; Nakanishi, K.; Turro N. Quantitative Aspects of the Photochemistry of Isomeric Retinals and Visual Pigments. *J. Am. Chem. Soc.* **1976**, *98*, 4189-4192.
- ³⁸ Loevsky, B.; Wand, A.; Bismuth, O.; Friedman, N.; Sheves, M.; and Ruhman, S. A new spectral window on Retinal Protein Photochemistry *J. Am. Chem. Soc.* **2011**, *133*, 1626-1629.
- ³⁹ Malhado, J.-P.; Spezia, R.; Hynes, J. T. Dynamical Friction Effects on the Photoisomerization of a Model Protonated Schiff Base in Solution. *J. Phys. Chem. A* **2011**, *115*, 3720-3735.

- ⁴⁰ Doukas, A. G.; Junnarkar M. R.; Alfano R. R.; Callender R. H.; Kakitani T.; Honig B. Fluorescence quantum yield of visual pigments: Evidence of subpicosecond isomerization rates. *Proc. Natl. Acad. Sci. U.S.A.* **1984**, *81*, 4790-4794.
- ⁴¹ Blum, K. *Density Matrix Theory and Applications* (Plenum Press, New York) **1981**, chap. 7.
- ⁴² May, V., Kühn, O. *Charge and Energy Transfer Dynamics in Molecular Systems* (Wiley-VCH Verlag GmbH & Co. KGaA, Weinheim) **2004**, chap. 3.
- ⁴³ See Supplementary Material for plots of probability distributions shown in Figs. 7 and 9 integrated over the coupling mode x .
- ⁴⁴ Berkelbach T. C.; Hybertsen M. S.; Reichman D. R. Microscopic theory of singlet exciton fission. I. General formulation *J. Chem. Phys.* **2013**, *138*, 114102-1-114102-16.
- ⁴⁵ Hahn S.; Stock, G. Ultrafast *cis-trans* photoswitching: A model study *J. Chem. Phys.* **2002**, *138*, 1085-1091.

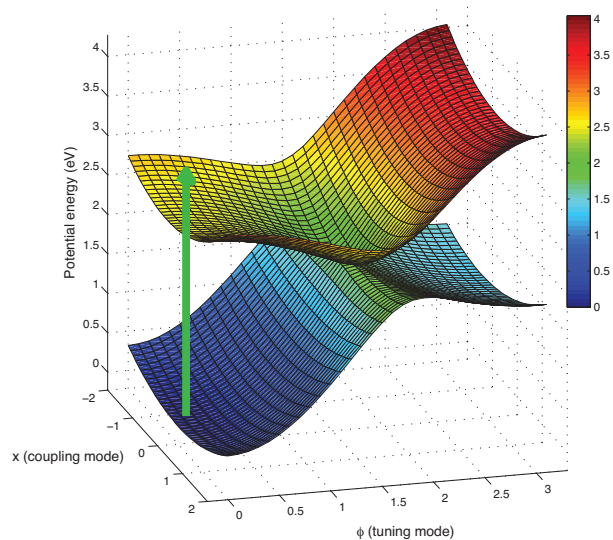
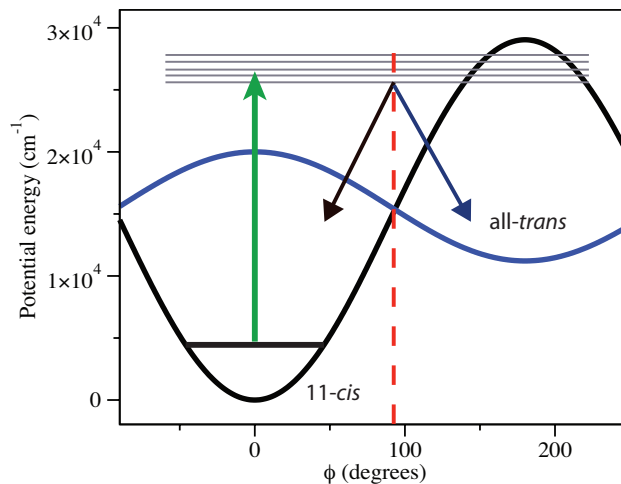


Fig. 1: (Upper panel) Ground and first excited diabatic potential profiles along the reaction coordinate ϕ for retinal photoisomerization. The green upward arrow illustrates laser excitation, the downward arrows illustrate the partitioning of the eigenstates into *cis* and *trans* (by the projection operators, see text). The *cis* and *trans* regions of configuration space are separated by the red dashed line. (Lower panel) Adiabatic PESs for retinal as functions of the torsional coordinate ϕ and the coupling mode x orthogonal to it. The PESs are obtained by diagonalizing the Hamiltonian in Eq. (12) (without the kinetic energy term).

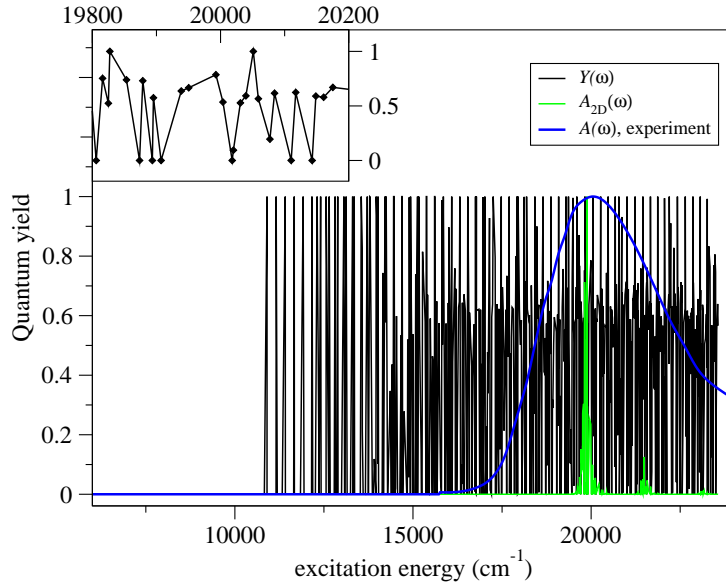


Fig. 2: Frequency dependence of the stationary quantum yield. Superimposed on the plot are the linear absorption spectrum of the 2D model (green) and the experimental absorption spectrum spectrum of retinal in rhodopsin adapted from Fig. 2 of Ref. 23, both normalized to unity at their respective maxima. The inset shows an expanded view of the frequency-dependent quantum yield in the region of maximum absorption at $\omega \sim 20,000 \text{ cm}^{-1}$ ($\lambda = 500 \text{ nm}$)

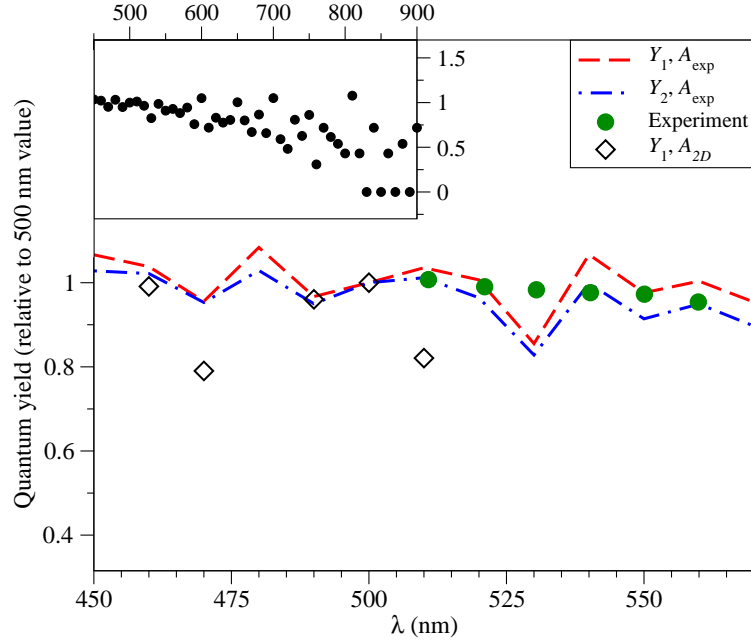


Fig. 3: Wavelength dependence of the stationary quantum yield. Diamonds – results for $A_{2D}(\omega)$ calculated from the two-state two-mode model; dashed (dash-dotted) lines – results obtained for Y_1 (Y_2) and the experimentally measured $A(\omega)$ ¹¹, circles – experiment. The error bars are smaller than the size of the circles. The inset shows the bare frequency-dependent quantum yield (16) calculated *without* the spectral lineshape function $A(\omega)$. The experimental quantum yield stays constant below $\lambda = 500$ nm. The results for $A_{2D}(\omega)$ are shown only in those spectral regions where $A_{2D}(\omega)$ does not vanish (see Fig. 2).

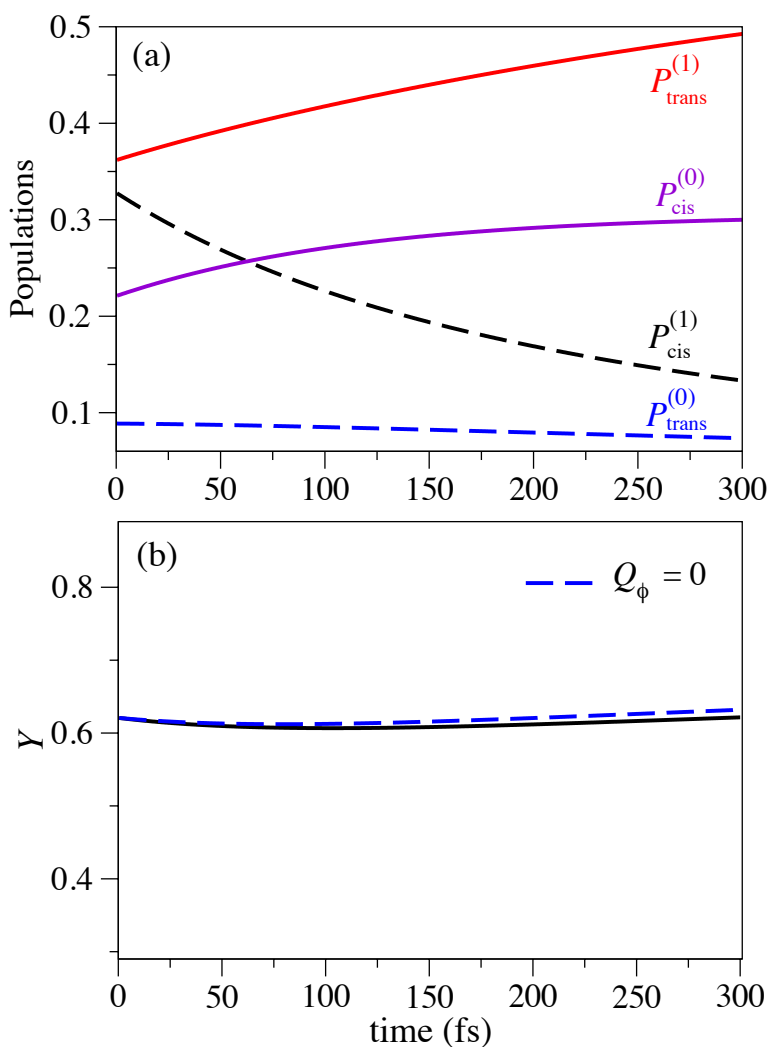


Fig. 4: (a) Time dependence of *cis* and *trans* state populations (see Eq. 2). The excited-state populations $P_{\text{cis}}^{(1)}$ and $P_{\text{trans}}^{(0)}$ (dashed lines) decay in time due to the interaction with the environment (see text). (b) Time dependence of the quantum yield given by Eq. (1). These results are obtained by solving the equations of motion for the diagonal elements of the density matrix parametrized by the transition rates given by Eqs. (17)-(18). The quantum yield remains constant (within 3% of the asymptotic value of 0.62) over the time interval $0 < t < 3000$ fs.

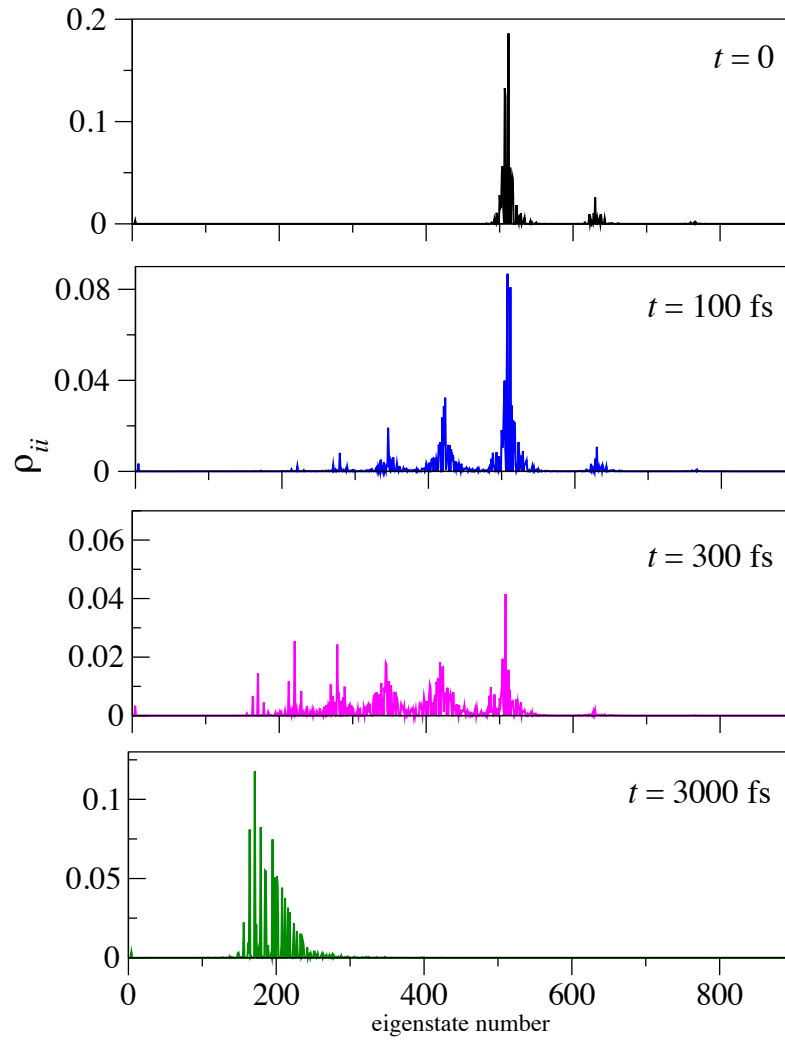


Fig. 5: Snapshots of eigenstate populations $\rho_{ii}(t)$. At $t = 0$, the bright eigenstates (mostly 512, 507, and 508) are populated by fully incoherent, impulsive FC excitation (see Eq. 6). At later times, interaction with the bath causes the population of the bright states to decay through several cascades (middle panels). The resulting steady-state eigenstate distribution is plotted in the lowermost panel.

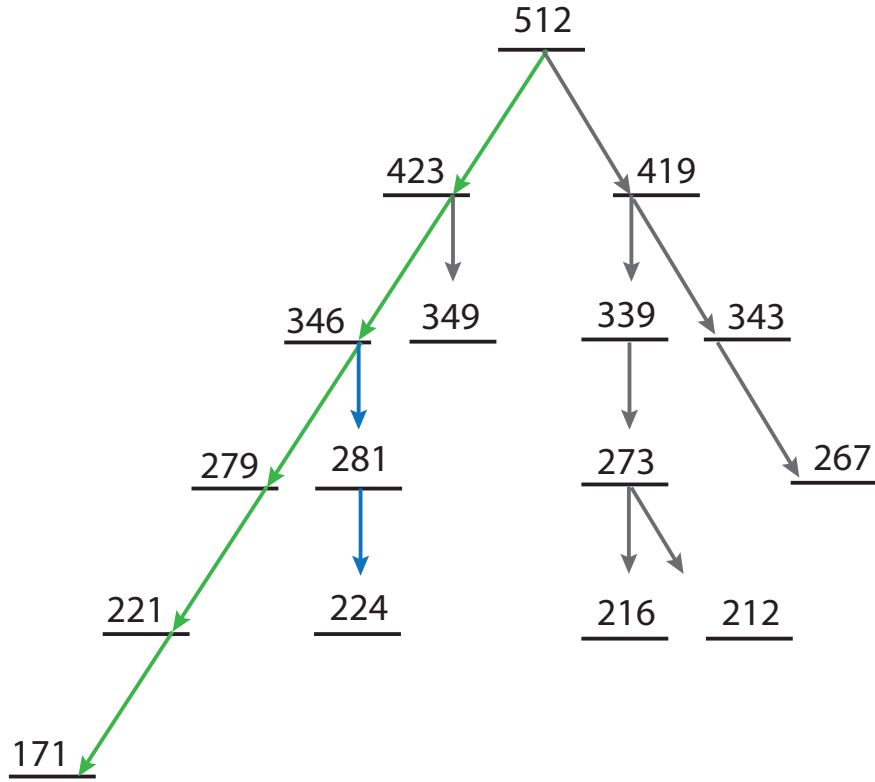


Fig. 6: The network of dominant relaxation pathways starting from the dominant bright state $|512\rangle$ (the highest peak in the upper panel of Fig. 5). Green arrows show the most efficient pathway leading to the $|171\rangle$ eigenstate (the highest peak in the lower panel of Fig. 6). See text for details.

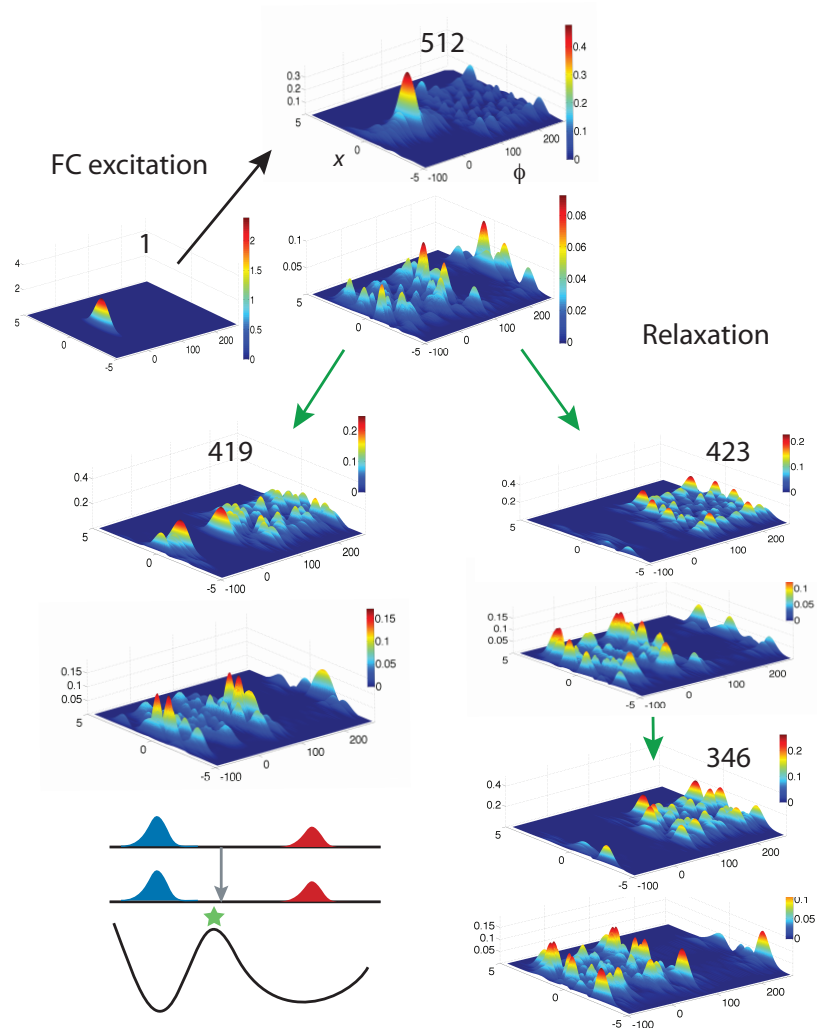


Fig. 7: Probability density (Eq. 20) for the ground ($n = 0$, upper panels) and the first excited ($n = 1$, lower panels) diabatic electronic states as a function of the torsional coordinate ϕ and the coupling mode x . Only the eigenstates above the conical intersection are shown. Note the similarity of the ϕ -profiles of the eigenstates involved in the relaxation process, which implies no change in the quantum yield. The lower left figure illustrates that *cis/trans* partitioning of delocalized eigenstates above the conical intersection (marked by the star) does not change qualitatively during relaxation. Note changes in color scale from panel to panel.

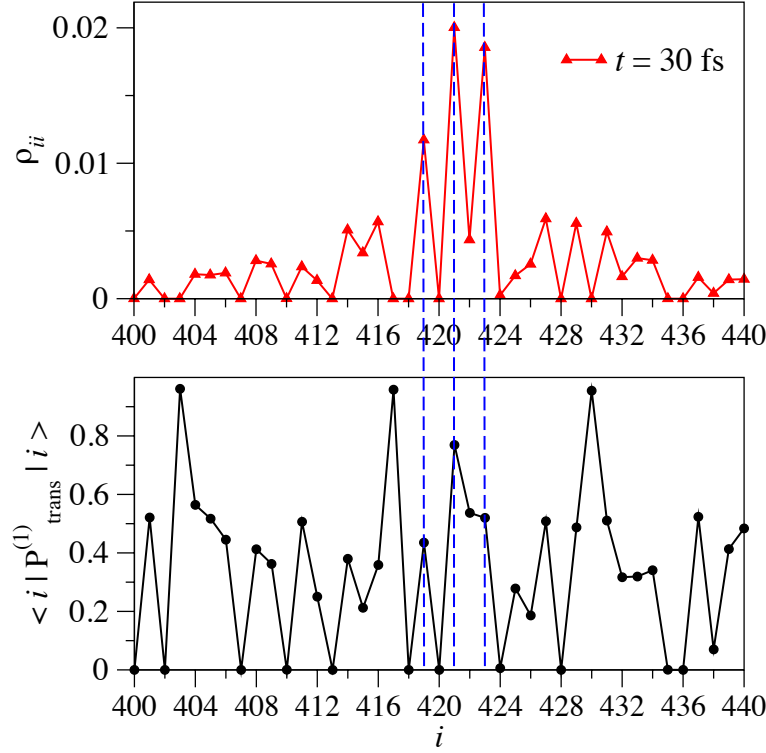


Fig. 8: Localization properties of the eigenstates in the first relaxation cascade. (Upper panel): the populations of the first-cascade eigenstates at $t = 30$ fs after the initial excitation. (Lower panel): the diagonal matrix element of the projection operator $\hat{P}_{\text{trans}}^{(1)}$ quantifying the amount of population in the *trans*-region of configuration space. Note that all eigenstates significantly populated in the first stage of relaxation have similar localization properties with $\langle i | P_{\text{trans}}^{(1)} | i \rangle = 0.36 - 0.56$. Notable exceptions include states $|421\rangle$ and $|415\rangle$ with $\langle 421 | P_{\text{trans}}^{(1)} | 421 \rangle = 0.76$ and $\langle 415 | P_{\text{trans}}^{(1)} | 415 \rangle = 0.21$.

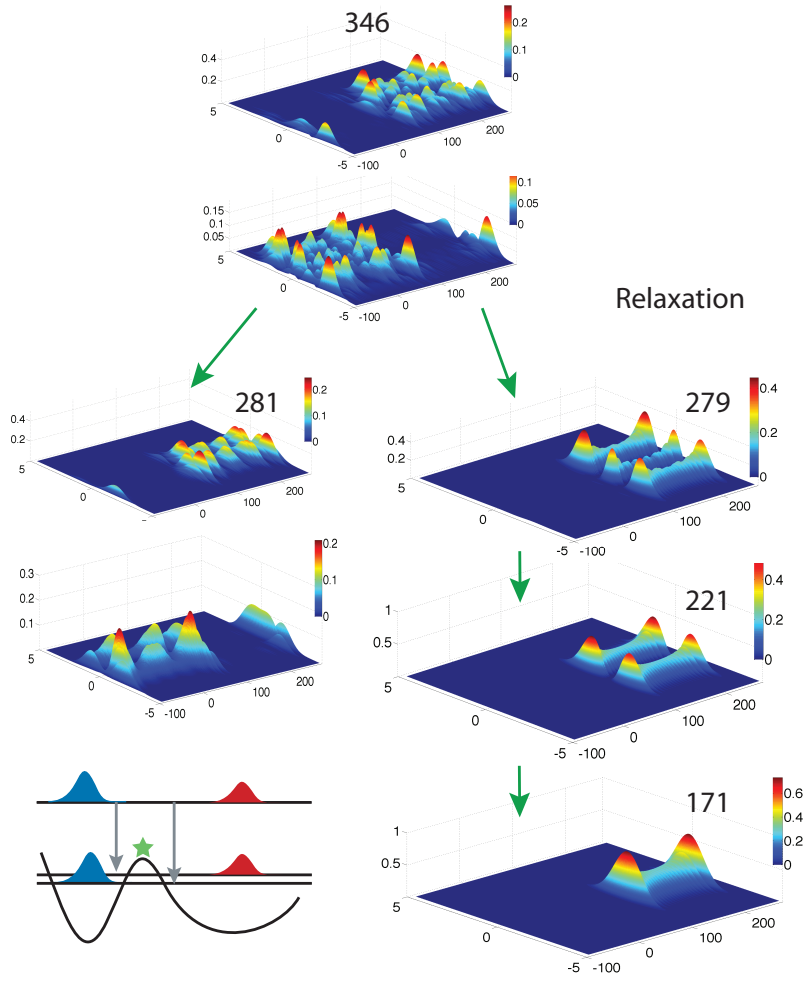


Fig. 9 Same as in Fig. 7 but for the eigenstates in the vicinity of and below the conical intersection. Note the different localization properties of the eigenstates involved in the relaxation process. The lower left figure illustrates the transition from delocalized to localized eigenstates below the conical intersection (marked by the star). Note changes in color scale from panel to panel.